Scripta Materialia 148 (2018) 5–9

Contents lists available at ScienceDirect

Scripta Materialia

journal homepage: www.elsevier.com/locate/scriptamat

Regular article

Microstructure and mechanical behavior of nanotwinned AlTi alloys with 9R phase

Y.F. Zhang [a], S. Xue [a], Q. Li [a], C. Fan [a], R. Su [a], Jie Ding [a], Han Wang [a], H. Wang [a,b], X. Zhang [a,*]

[a] School of Materials Engineering, Purdue University, West Lafayette, IN 47907, United States
[b] School of Electrical and Computer Engineering, Purdue University, West Lafayette, IN 47907, United States

ARTICLE INFO

Article history:
Received 24 November 2017
Received in revised form 22 December 2017
Accepted 8 January 2018
Available online xxxx

Keywords:
Aluminum alloys
Thin film
Sputtering
Nanoindentation
ITB and 9R

ABSTRACT

Nanotwinned metals have shown high strength and ductility. However, metals with high stacking fault energy, such as Al, typically do not contain high-density growth twins or stacking faults. Here we show that by using a small amount of Ti solutes, 0.15–5.1 at.%, fine grains with a large population of extended incoherent twin boundaries bounding broad 9R phase form in sputtered AlTi films. These nanotwinned AlTi films have hardness as high as 2 GPa. This study provides an alternative approach to design high-strength Al alloys by grain refinement and introducing high-density twin boundaries and 9R phase.

Published by Elsevier Ltd on behalf of Acta Materialia Inc.

Recently, extensive studies have revealed that nanotwinned (nt) metals have high strength and ductility [1–6], thermal stability [7–9], and good electrical conductivity [10,11]. Most prior studies on nt metals focused on metals with low stacking fault energy (SFE), such as Ag [12], 304 stainless steel [13], and Cu [1–3,9,14,15], where growth twins readily form. In these nt metals with low SFE, Σ3 (111) coherent twin boundaries (CTBs) have low-energy and symmetrical configuration [16], and can serve as strong barriers to the transmission of dislocations, as shown by molecular dynamics (MD) simulations [17,18] and *in situ* studies [19]. In addition to CTBs, Σ3 (112) incoherent twin boundaries (ITBs) also play a crucial role in the deformation process of nt metals.

Growth twins are difficult to form in Al due to its high SFE (120–166 mJ/m^2 [20]). Recently, by using Ag as a seed layer, Bufford et al. successfully fabricated nt Al with high-density growth twins [21,22]. A majority of these twins are ITBs. Xue et al. [23], by means of DC magnetron sputtering, synthesized polycrystalline ultra-fine grained Al thin films with nearly 10% twinned grains by controlling the film thickness without using any seed layer. These Al films have abundant ITBs, which can be explained by twin nucleation and growth mechanism [23] and relative small ITB/CTB [24–26]energy ratio (~3.5) in Al when compared with Ag (~16 mJ/m^2) or Cu (~22 mJ/m^2) [22]. MD simulations also predicted that the deformation response of ITBs depends on the SFE of a metallic material [25,27]. *In situ* nanoindentation studies show that ITBs in Al are strong barriers to the pile-up of dislocations, leading to significant work hardening [28]. High-resolution transmission electron microscopy (HRTEM) [16,24,29,30] and atomistic simulations [16,25] have been used to study the microstructure of ITBs in face-centered cubic (FCC) metals.

In this work, by adding a small amount of Ti (0.15–5.1 at.%) into Al, we introduced high-density ITBs and unexpectedly broad 9R phase into sputtered AlTi films. High-density TBs lead to remarkable hardness enhancement in these highly twinned AlTi films. This study suggests that the introduction of ITBs and 9R phase into Al can be an alternative method to design high-strength and light-weight Al alloys.

At room temperature, 1.0 μm thick AlTi thin films with 80 nm thick Ag seed layers were deposited on (Hydrofluoric acid) HF etched Si (111) substrates, by DC magnetron sputtering using Al (99.99%), Ti (99.99%) and Ag (99.99%) targets. Before deposition, the base pressure of the vacuum chamber was below 4×10^{-8} Torr. The Ar pressure was 1×10^{-3} Torr during sputtering. X-ray diffraction experiments (out-of-plane θ-2θ scans, in-plane {111} phi scans, pole-figure analyses) were used to examine the texture and quality of films, operated on a Panalytical Empyrean X'pert PRO MRD diffractometer. Plan-view and cross-section transmission electron microscopy (TEM) studies were performed on FEI Tecnai G2 F20 and Talos 200X analytical microscopes operated at 200 kV. Compositions of AlTi films were determined by using energy dispersive spectroscopy (EDS) on an FEI quanta 3D FEG scanning electron microscope. Hardness and elastic modulus tests were conducted on a Fischerscope 2000XYp nano/micro-indenter at different indentation depths by using instrumented nanoindentation method [31]. To avoid substrate effect, the maximum indentation depths were no more than 15% of the total film thickness.

* Corresponding author.
E-mail address: xzhang98@purdue.edu (X. Zhang).

https://doi.org/10.1016/j.scriptamat.2018.01.010
1359-6462/Published by Elsevier Ltd on behalf of Acta Materialia Inc.

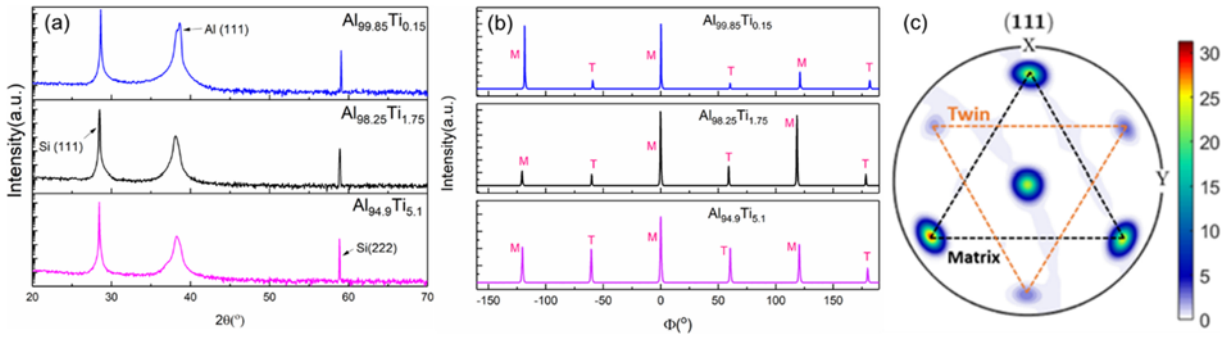

Fig. 1. (a) XRD profiles of sputtered AlTi films with peak intensity in logarithmic scale. (b) XRD {111} Phi scan profiles of AlTi thin films with different compositions. (c) XRD (111) pole figure analysis of the $Al_{94.9}Ti_{5.1}$ thin films.

As illustrated in Fig. 1a, as-deposited AlTi thin films have strong {111} texture. Small peaks beside the Al {111} peaks come from Ag seed layer, as Ag has similar lattice parameter compared to Al. In addition, there is no evidence showing the existence of Al-Ti or Al-Ag intermetallics. In-plane {111} Phi scan profiles (Fig. 1b) show two sets of peaks, including three peaks from the matrix (marked as M) and the other three peaks from the twins (marked as T). The twin/matrix peak intensity ratio increases with increasing Ti composition. 6-fold symmetrical dots appear on the pole figure profiles of $Al_{94.9}Ti_{5.1}$ (Fig. 1c), revealing the existence of growth twins in the {111} textured AlTi films.

Plan-view TEM micrographs (Fig. 2a–c) were obtained from Al <111> zone axis and the corresponding selected area diffraction (SAD) patterns further reveal the formation of {111} highly textured films. As shown in Fig. 2a, the $Al_{99.85}Ti_{0.15}$ film has hexagonal and polygonal giant grains with an average grain size of 1900 nm. Increasing Ti composition from 0.15 to 5.1% leads to the reduction of average grain size to 180 nm, as shown in the statistics of grain size distributions (Fig. 2d–f).

Bright-field cross section TEM (XTEM) micrographs (Fig. 3) were obtained from Al ⟨110⟩ zone axis. As shown in Fig. 3a, twin islands, with a width of >400 nm, were embedded within $Al_{99.85}Ti_{0.15}$ matrix. A small number of dislocations appeared near the interface between AlTi and Ag seed layer. The inserted SAD pattern taken from the red dotted circle (Fig. 3a) shows two sets of diffraction spots arising from twins and matrix respectively. The additional diffraction spots on the position of 1/3 {111} in reciprocal space originate from Σ3{112} ITBs. The magnified TEM micrograph in Fig.3b shows the formation of giant twins (bounded with extended ITBs) that spread more than 150 nm. Interestingly, the width of ITBs decreases along the growth direction. Meanwhile small but prominent steps appeared near ITBs, which are marked with blue dotted lines. In addition, high-resolution TEM (HRTEM) image in Fig.3c shows a narrow and straight ITB consisting of an array of partial dislocations in the sequence of b_2:b_1:b_3 [16]. A broad 9R phase is shown in HRTEM micrograph in Fig. 3d, as confirmed by the inserted fast Fourier transform (FFT) of the micrograph.

Low-magnification XTEM image (Fig. 3e) reveals much smaller columns with high-density dislocations in $Al_{94.9}Ti_{5.1}$ films. Similarly, inserted SAD pattern confirms the existence of ITBs. Also, the superimposed EDS mapping data show insignificant interdiffusion between Ag seed layer and AlTi films. Noticeably, the density of dislocations and SFs decreases along the film growth direction. Considering the nearly epitaxial growth of AlTi film over Ag seed layer, those dislocations and SFs may nucleate from the interface between the two layers [21]. As shown in Fig. 3g and h, a broad 9R phase (~160 nm in width) was embedded within the columns.

Fig.4 compiles the hardness data from literature [22,32–37] and this work. The horizontal gray dashed line indicates the hardness of the annealed of Al thin films [22], ~0.60 GPa, Increasing the Ti composition from 0.15 to 5.1% leads to a prominent hardness enhancement from

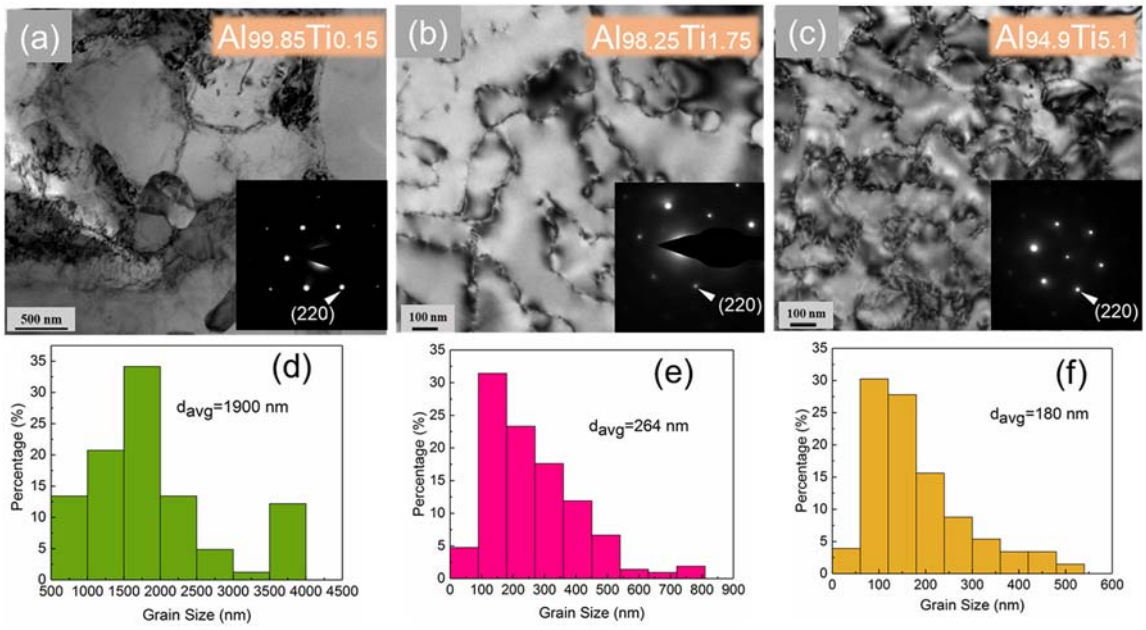

Fig. 2. (a–c) Plan-view TEM micrographs and the inserted selected area diffraction (SAD) patterns of AlTi alloy films with various compositions showing the formation of (111) highly textured films. (d–f) Statistics of grain size distributions show substantial grain refinement, from 1900 to 180 nm with increasing Ti concentration.

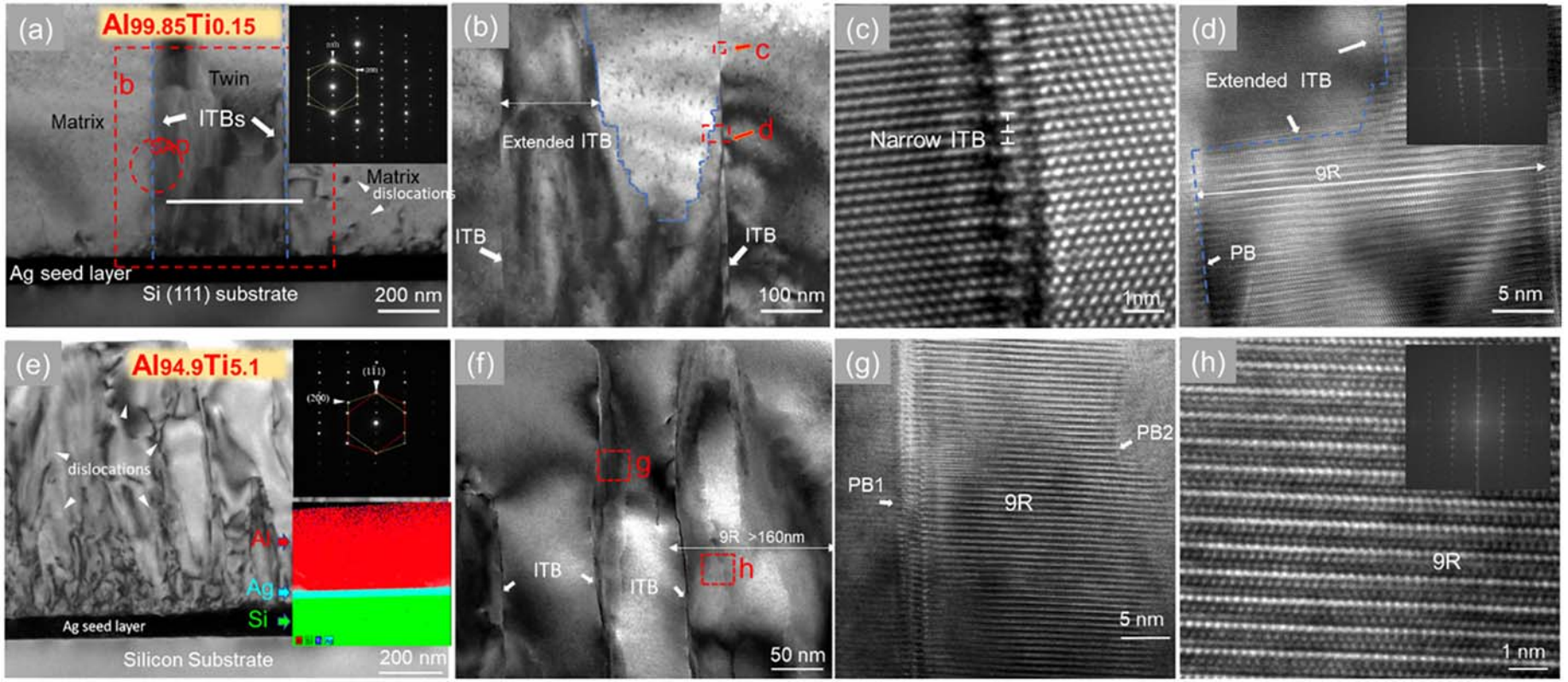

Fig. 3. Bright-field cross-section TEM (XTEM) image of $Al_{99.85}Ti_{0.15}$ (a–d) and $Al_{94.9}Ti_{5.1}$ (e–h) examined from Al ⟨011⟩ zone axis. (a) Twin islands embedded in the matrix. The inserted SAD pattern shows two sets of diffraction spots arising from the matrix and twin respectively, and additional spots arising from incoherent twin boundaries (ITBs). (b) Giant (broad) twins bounded by Σ3{112} ITBs (marked by blue lines). (c) Straight and narrow Σ3{112} ITBs. (d) Broad extended ITBs (or 9R phase). (e) Low magnification TEM image shows abundant columnar boundaries in $Al_{94.9}Ti_{5.1}$. The SAD pattern shows the formation of twins and ITBs. EDS mapping reveals no severe inter-diffusion between Ag seed layer (light blue) and AlTi film (red). Si is colored in green. (f) Broad intermingled 9R phase (>160 nm). Locations marked as g and h are shown in corresponding HRTEM micrographs. (g) Extended ITB bounding 9R phase with straight phase boundary (PB) 1 on the left and a curved PB2 on the right side. (h) Broad intermingled 9R phase (>160 nm) in the middle of the column. (For interpretation of the references to color in this figure legend, the reader is referred to the web version of this article.)

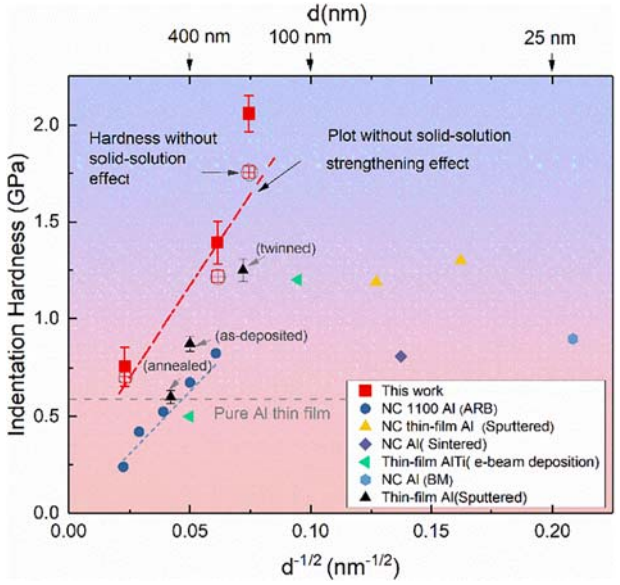

Fig. 4. Comparison of indentation hardness as a function of $d^{-1/2}$ (domain size) for AlTi film (in this work) and data from literature on epitaxial twined Al thin films [22], nanocrystalline (NC) bulk Al alloys [32–35]and thin films [36,37]. Hollow red blocks are hardness data points of AlTi thin film without the contribution from Ti solid-solution strengthening effect. The red dash line denotes the Hall–Petch slope of AlTi thin film excluding the solid-solution strengthening effect after calculation. The light blue line represents the Hall–Petch slope for the bulk NC alloys. (For interpretation of the references to color in this figure legend, the reader is referred to the web version of this article.)

0.76 to 2.1 GPa. The hardness values of bulk Al alloys are either measured by microhardness test [33,34] or converted from tensile strength by multiplying a Tabor factor [32,35].

Several factors may be responsible for the prominent increase in hardness of AlTi films, including solid solution effect [38–41], size effect [40,42], introduction of ITBs and 9R phase [14,22,28]. The following discussions will show that the hardness increase arises primarily from the last two factors.

Solid solution strengthening comes from the interaction between mobile dislocations and stress fields induced by solutes atoms [43]. The solid solution effect of substitutional solutes can be calculated by using Fleischer formulation [38,41]:

$$\Delta\tau = 0.0235 \cdot G_{solvent} \cdot \varepsilon_s^{3/2} \cdot c^{1/2}, \tag{1}$$

where, $\Delta\tau$ is the shear stress induced by solute atoms, $G_{solvent}$ is the shear modulus of Al(26.9 GPa [40]), c is the concentration of solute atoms. ε_s represents the interaction factor incorporating variations of lattice parameter and shear modulus and is defined as:

$$\varepsilon_s = \left| \frac{\frac{1}{G_{solvent}} \cdot \frac{dG}{dc}}{1 + \frac{1}{2}\left|\frac{1}{G_{solvent}} \cdot \frac{dG}{dc}\right|} - 3 \cdot \frac{1}{a_{solvent}} \cdot \frac{da}{dc} \right|, \tag{2}$$

where, G is the shear modulus of alloy, $a_{solvent}$ is the lattice parameter of Al (0.405 nm), a denotes the lattice parameter of alloy. We assume that, both the shear modulus and lattice parameter of AlTi alloy increase linearly with Ti concentration [43], then $\Delta\tau$ is estimated to be 0.036, 0.021 and 0.0062 GPa for $Al_{94.9}Ti_{5.1}$, $Al_{98.25}Ti_{1.75}$, and $Al_{99.85}Ti_{0.15}$ respectively. Using Eqs. (1) and (2), considering Tabor factor of 2.7 [44] and Taylor factor of 3.1 [42], the calculated hardness contribution (ΔH) from solid solution can be calculated. Clearly the solid solution strengthening effect is insignificant and cannot explain the significant hardness increase in AlTi alloys.

Grain refinement can be an important strengthening mechanism for AlTi thin films. In general, the addition of Ti from 0.15 to 5.1 at.% decreases the average grain size of AlTi thin film from 1900 to 180 nm. XTEM studies suggest that island nucleation and growth mechanisms [45] dominate during the deposition of AlTi films. The addition of Ti would lower the mobility and diffusivity of Al atoms [46–48], and thus, shorten the diffusion distance of Al atoms, resulting in higher nuclei density and smaller grain size [49].

The grain size induced strengthening effect can be described by the well-known Hall–Petch equation [40,43]:$\sigma_y = \sigma_0 + K_y d^{-1/2}$.Where σ_0 is the friction stress, K_y is Hall–Petch slope, and d is the average grain diameter. K_y reflects the barrier strength from grain boundaries to the transmission of dislocations. As illustrated in Fig.4., the red dashed line denotes the Hall–Petch slope of AlTi thin films that excludes the solid solution strengthening effect (subtracting the hardness increase due to solid solution strengthening). The Hall–Petch slope of AlTi thin films, divided by a Tabor factor of 2.7, is ~6.9 GPa$\sqrt{\text{nm}}$. In comparison, the Hall–Petch slope extracted from the plot of NC Al [35] alloy is nearly 4.8 GPa$\sqrt{\text{nm}}$. Compared with NC Al, the larger Hall–Petch slope indicates a stronger barrier strength of grain boundaries in AlTi thin films. The sputtered AlTi films have a high density of ITBs, and hence it is likely that TBs dominate the strength of these films. MD simulations and *in situ* nanoindentation studies [28] show that ITBs in nanotwinned Al can effectively resist the pile-up of dislocations and lead to significant work hardening. In addition, *in situ* nanoindentation [28] also shows that the stress needed for a dislocation to transmit across the ITBs is ~300 MPa for nanotwinned Al.

Based on the measured Hall–Petch plot, we estimated the peak strength of twinned AlTi thin film by using the following equation [12]:

$$\tau^* = \left(\frac{K_{HP}\pi(1-\nu)}{Gb}\right), \tag{3}$$

where τ^* is boundary barrier strength, K_{HP} is the Hall–Petch slope for resolved shear stress, ν is the Poisson's ratio (0.35 for Al [28]), G is the shear modulus of Al (26.9 GPa [40]), and b is the magnitude of Burgers vector of a perfect dislocation in Al (0.286 nm). The calculated $\tau^*$of twinned AlTi thin film is ~1.3 GPa, and once multiplied by the Tabor [44] and Taylor factor [42], the peak hardness of the film is predicted to be ~10.9 GPa. Thus, the AlTi thin films in this study achieves ~20% of the predicted peak hardness, due to large grain sizes. Further hardness enhancement might be accomplished by significantly reducing the average grain size or increasing twin density.

Next, we examine the influence of TBs on the high hardness of AlTi solid solution alloy films. TEM studies show that sputtered AlTi alloy films contain high-density broad 9R phase. Many of the columnar grains are entirely consisted of 9R phase. As shown in Fig. 4, for a similar grain size, the hardness of AlTi solid solution films is at least 0.5–1 GPa greater than that of Al with conventional high angle grain boundaries [35]. Such a drastic difference in hardness cannot be accounted by solid solution strengthening or the increase of friction stress. The high hardness of AlTi films (compared to Al with the same grain size) indicates that ITBs and 9R phase can effectively improve the barrier strength of Al alloys to transmission of dislocations. Careful examination of Fig. 4 also shows that the Hall–Petch slope for AlTi films is greater than that of conventional polycrystalline Al. Such a slope difference also suggests that the broad 9R phase poses a strong barrier for the transmission of dislocations, and hence leads to strengthening in sputtered AlTi films. A recent study [50] shows that 9R phase can also be generated in Al-Fe solid solution alloy films (with a few atomic percent of Fe). The nanograins and high density ITBs lead to remarkable increase in films hardness (>5 GPa). MD simulations show that 9R can indeed resist the transmission of dislocations in twinned AlFe solid solution films.

Finally, we evaluate the mechanism for the formation of 9R phase in AlTi solid solution alloys. As illustrated before, the formation of 9R phase is a result of dissociation of narrow ITBs by emission of partial

dislocations on every three {111} planes [51]. In the dislocation model of an ITB in FCC metal, b_2 and b_3 are mixed Shockley partial dislocations with a Burgers vector of $\frac{1}{6}[\bar{2}11]$ and $\frac{1}{6}[1\bar{2}1]$ respectively. While, b_1 is an edge dislocation that has a Burgers vector of $\frac{1}{6}[11\bar{2}]$ [16,25,51]. Because of their opposite screw components, b_2 and b_3 will attract each other, making them more difficult to move compared with b_1. Consequently, under shear stress, b_2 and b_3 tend to bond with each other and move slowly, while b_1 slips away rapidly from initial compact ITB on {111} plane.

Though 9R phase of several nm wide has been found in as-deposited Al film [22] or under high strain rate deformation of Al [52], it is rare to observe giant 9R phase with width of >100 nm in Al alloys. The formation of giant 9R phase may be interpreted from several aspects. (1) Stacking fault energy (SFE) reduction. According to the density function theory calculation [53], the addition of Ti can lower the SFE of Al by changing the directional charge distribution in Al. Specifically, around 38% reduction in SFE of Al can be achieved by adding 3.3% Ti atoms. Thus, the addition of Ti may promote the formation of TBs and broad 9R phase. (2) Local stress state. The local stress state is complex and varies at different positions within films during deposition process [54]. In the island growth process, there is a local shear stress between substrate and film arising from the edge of the islands. The shear stress has been estimated to be ~0.5–1 GPa in Al [22], which may be sufficient to cause the dissociation of compact ITBs into 9R phase [55]. (3) Non-equilibrium sputtering process and stabilization of 9R phase by Ti atoms. DC magnetron sputtering is a type of physical vapor deposition (PVD) process, [45,54,56], where rapid quenching may facilitate the formation of growth defects, such as 9R phase within the films. Furthermore, the presence of Ti impurity atoms may stabilize the 9R phase by pining partial dislocations (preventing detwinning).

In summary, by using magnetron sputtering, we fabricated highly textured AlTi thin films with high-density broad 9R phase. The hardness of twinned AlTi films reaches 2 GPa. The high strength arises mainly from the high-density ITBs, broad 9R phase and fine grains. This work provides an alternative method to design high-strength and light-weight Al alloys by introducing ITBs and broad 9R phase.

Acknowledgement

This work is supported by the Department of Energy-Office of Basic Energy Sciences (grant number: DE-SC0016337); H. W acknowledges financial support by the Office of Naval Research (s (N000141612778 and N000141712087)) program managed by Dr. Antti Makinen. J. D acknowledges support from the DOE-Nuclear Energy under DE-NE0008549.

References

[1] X. Li, Y. Wei, L. Lu, K. Lu, H. Gao, Nature 464 (2010) 877–880.
[2] K. Lu, L. Lu, S. Suresh, Science 324 (2009) 349 (80-.).
[3] L. Lu, X. Chen, X. Huang, K. Lu, Science 323 (2009) 607 (80-.).
[4] J. Wang, F. Sansoz, J. Huang, Y. Liu, S. Sun, Z. Zhang, S.X. Mao, Nat. Commun. 4 (2013) 1742.
[5] J. Wang, X. Zhang, MRS Bull. 41 (2016) 274–281.
[6] Y.M. Wang, F. Sansoz, T. LaGrange, R.T. Ott, J. Marian, T.W. Barbee Jr, A.V. Hamza, Nat. Mater. 12 (2013) 697–702.
[7] O. Anderoglu, A. Misra, H. Wang, F. Ronning, M.F. Hundley, X. Zhang, Appl. Phys. Lett. 93 (2008) 83108.
[8] J.A. Brown, N.M. Ghoniem, Acta Mater. 57 (2009) 4454–4462.
[9] X. Zhang, A. Misra, Scr. Mater. 66 (2012) 860–865.
[10] O. Anderoglu, A. Misra, H. Wang, X. Zhang, J. Appl. Phys. 103 (2008) 94322.
[11] L. Lu, Y. Shen, X. Chen, L. Qian, K. Lu, Science 304 (2004) 422–426 (80-.).
[12] D. Bufford, H. Wang, X. Zhang, Acta Mater. 59 (2011) 93–101.
[13] X. Zhang, A. Misra, H. Wang, T.D. Shen, M. Nastasi, T.E. Mitchell, J.P. Hirth, R.G. Hoagland, J.D. Embury, Acta Mater. 52 (2004) 995–1002.
[14] X. Zhang, A. Misra, H. Wang, M. Nastasi, J.D. Embury, T.E. Mitchell, R.G. Hoagland, J.P. Hirth, Appl. Phys. Lett. 84 (2004) 1096–1098.
[15] A.M. Hodge, T.A. Furnish, C.J. Shute, Y. Liao, X. Huang, C.S. Hong, Y.T. Zhu, T.W. Barbee Jr, J.R. Weertman, Scr. Mater. 66 (2012) 872–877.
[16] J. Wang, O. Anderoglu, J.P. Hirth, A. Misra, X. Zhang, Appl. Phys. Lett. 95 (2009) 21908.
[17] Z.-H. Jin, P. Gumbsch, K. Albe, E. Ma, K. Lu, H. Gleiter, H. Hahn, Acta Mater. 56 (2008) 1126–1135.
[18] Z.-H. Jin, P. Gumbsch, E. Ma, K. Albe, K. Lu, H. Hahn, H. Gleiter, Scr. Mater. 54 (2006) 1163–1168.
[19] Y.B. Wang, M.L. Sui, Appl. Phys. Lett. 94 (2009) 21909.
[20] M. Chen, E. Ma, K.J. Hemker, H. Sheng, Y. Wang, X. Cheng, Science 300 (2003) 1275–1277 (80-.).
[21] D. Bufford, Z. Bi, Q.X. Jia, H. Wang, X. Zhang, Appl. Phys. Lett. 101 (2012) 223112.
[22] D. Bufford, Y. Liu, Y. Zhu, Z. Bi, Q.X. Jia, H. Wang, X. Zhang, Mater. Res. Lett. 1 (2013) 51–60.
[23] S. Xue, Z. Fan, Y. Chen, J. Li, H. Wang, X. Zhang, Acta Mater. 101 (2015) 62–70.
[24] D.L. Medlin, M.J. Mills, W.M. Stobbs, M.S. Daw, F. Cosandey, MRS Proc, Cambridge Univ Press, 1992 91.
[25] J. Wang, A. Misra, J.P. Hirth, Phys. Rev. B 83 (2011) 64106.
[26] L.E. Murr, (1975).
[27] J. Wang, N. Li, O. Anderoglu, X. Zhang, A. Misra, J.Y. Huang, J.P. Hirth, Acta Mater. 58 (2010) 2262–2270.
[28] D. Bufford, Y. Liu, J. Wang, H. Wang, X. Zhang, Nat. Commun. 5 (2014).
[29] D. Hofmann, F. Ernst, Ultramicroscopy 53 (1994) 205–221.
[30] J.M. Pénisson, U. Dahmen, M.J. Mills, Philos. Mag. Lett. 64 (1991) 277–283.
[31] G.M. Pharr, W.C. Oliver, MRS Bull. 17 (1992) 28–33.
[32] K. Il Moon, M.S. Oh, K.S. Lee, J. Alloys Compd. 302 (2000) 227–234.
[33] K.V. Rajulapati, R.O. Scattergood, K.L. Murty, G. Duscher, C.C. Koch, Scr. Mater. 55 (2006) 155–158.
[34] X.K. Sun, H.T. Cong, M.C. Yang, M. Sun, Metall. Mater. Trans. A 31 (2000) 1017–1024.
[35] N. Tsuji, Y. Ito, Y. Saito, Y. Minamino, Scr. Mater. 47 (2002) 893–899.
[36] A.G. Dirks, T. Tien, J.M. Towner, J. Appl. Phys. 59 (1986) 2010–2014.
[37] D.S. Gianola, S. Van Petegem, M. Legros, S. Brandstetter, H. Van Swygenhoven, K.J. Hemker, Acta Mater. 54 (2006) 2253–2263.
[38] R.L. Fleischer, Acta Metall. 11 (1963) 203–209.
[39] R.L. Fleischer, Acta Metall. 10 (1962) 835–842.
[40] K. Ma, H. Wen, T. Hu, T.D. Topping, D. Isheim, D.N. Seidman, E.J. Lavernia, J.M. Schoenung, Acta Mater. 62 (2014) 141–155.
[41] T.J. Rupert, J.C. Trenkle, C.A. Schuh, Acta Mater. 59 (2011) 1619–1631.
[42] A. Misra, J.P. Hirth, R.G. Hoagland, Acta Mater. 53 (2005) 4817–4824.
[43] T.H. Courtney, Mechanical Behavior of Materials, Waveland Press, 2005.
[44] M. Mata, M. Anglada, J. Alcalá, J. Mater. Res. 17 (2002) 964–976.
[45] J.A. Venables, G.D.T. Spiller, M. Hanbucken, Rep. Prog. Phys. 47 (1984) 399.
[46] Y. Mishin, C. Herzig, Acta Mater. 48 (2000) 589–623.
[47] S.-Y. Lee, O. Taguchi, Y. Iijima, Mater. Trans. 51 (2010) 1809–1813.
[48] J.A.M. Antonio, L.F.M. Lfo, Metall. Trans. 2 (1971) 465–471.
[49] Z. Zhang, M.G. Lagally, Science 276 (1997) 377–383 (80-.).
[50] Q. Li, S. Xue, J. Wang, S. Shao, A.H. Kwong, Z. Fan, Y. Liu, Z. Qi, J. Ding, Han Wang, J.R. Greer, H. Wang, X. Zhang, Adv. Mater. (2018) in press.
[51] D.L. Medlin, G.H. Campbell, C.B. Carter, Acta Mater. 46 (1998) 5135–5142.
[52] Sichuang Xue, Zhe Fan, Olawale B. Lawal, Ramathasan Thevamaran, Qiang Li, Yue Liu, K.Y. Yu, Jian Wang, Edwin L. Thomas, Haiyan Wang, Xinghang Zhang, Nat. Commun. 8 (1653) (2017)https://doi.org/10.1038/s41467-017-01729-4.
[53] Y. Qi, R.K. Mishra, Phys. Rev. B 75 (2007) 224105.
[54] L. Ben Freund, S. Suresh, Thin Film Materials: Stress, Defect Formation and Surface Evolution, Cambridge University Press, 2004.
[55] G.H. Campbell, D.K. Chan, D.L. Medlin, J.E. Angelo, C.B. Carter, Scr. Mater. 35 (1996) 837–842.
[56] X. Zhang, O. Anderoglu, A. Misra, H. Wang, Appl. Phys. Lett. 90 (2007) 153101.